

OGLE-2014-BLG-0319: A Sub-Jupiter-Mass Planetary Event Encountered Degeneracy with Different Mass Ratios and Lens-Source Relative Proper Motions

SHOTA MIYAZAKI,^{1,*} DAISUKE SUZUKI,^{1,*} ANDRZEJ UDALSKI,^{2,†} NAOKI KOSHIMOTO,^{3,4,*} DAVID P. BENNETT,^{3,4,*}
 NICHOLAS RATTENBURY,^{5,*} TAKAHIRO SUMI,^{1,*}

(LEADING AUTHORS)

FUMIO ABE,⁶ RICHARD K. BARRY,³ APARNA BHATTACHARYA,^{7,3} IAN A. BOND,⁸ AKIHIKO FUKUI,^{9,10} HIROSANE FUJII,¹
 YUKI HIRAO,¹ STELA ISHITANI SILVA,^{3,11} YOSHITAKA ITOW,¹² RINTARO KIRIKAWA,¹ IONA KONDO,¹ BRANDON MUNFORD,⁵
 YUTAKA MATSUBARA,¹² SHO MATSUMOTO,¹ YASUSHI MURAKI,¹² ARISA OKAMURA,¹ GREG OLMSCHENK,^{3,13}
 CLÉMENT RANC,¹⁴ YUKI K. SATOH,¹ TAIGA TODA,¹ PAUL J. TRISTRAM,¹⁵ HIBIKI YAMA,¹ ATSUNORI YONEHARA,¹⁶

(MOA COLLABORATION)

RADEK POLESKI,² PRZEMEK MRÓZ,¹⁷ JAN SKOWRON,² MICHAL K. SZYMAŃSKI,² IGOR SOSZYŃSKI,² PAWEŁ PIETRUKOWICZ,²
 SYZMON KOZŁOWSKI,² KRZYSZTOF ULACZYK,^{2,18} ŁUKASZ WYRZYKOWSKI,²

(OGLE COLLABORATION)

¹Department of Earth and Space Science, Graduate School of Science, Osaka University, 1-1 Machikaneyama, Toyonaka, Osaka 560-0043, Japan

²Astronomical Observatory, University of Warsaw, Al. Ujazdowskie 4, 00-478 Warszawa, Poland

³Code 667, NASA Goddard Space Flight Center, Greenbelt, MD 20771, USA

⁴Department of Astronomy, University of Maryland, College Park, MD 20742, USA

⁵Department of Physics, University of Auckland, Private Bag 92019, Auckland, New Zealand

⁶Institute for Space-Earth Environmental Research, Nagoya University, Nagoya 464-8601, Japan

⁷Department of Physics, University of Notre Dame, Notre Dame, IN 46556, USA

⁸Institute of Information and Mathematical Sciences, Massey University, Private Bag 102-904, North Shore Mail Centre, Auckland, New Zealand

⁹Department of Earth and Planetary Science, Graduate School of Science, The University of Tokyo, 7-3-1 Hongo, Bunkyo-ku, Tokyo 113-0033, Japan

¹⁰Instituto de Astrofísica de Canarias, Vía Láctea s/n, E-38205 La Laguna, Tenerife, Spain

¹¹Department of Physics, The Catholic University of America, Washington, DC 20064, USA

¹²Institute for Space-Earth Environmental Research, Nagoya University, Nagoya, 464-8601, Japan

¹³Universities Space Research Association, Columbia, MD 21046, USA

¹⁴Sorbonne Université, CNRS, UMR 7095, Institut d’Astrophysique de Paris, 98 bis bd Arago, 75014 Paris, France

¹⁵University of Canterbury Mt. John Observatory, P.O. Box 56, Lake Tekapo 8770, New Zealand

¹⁶Department of Physics, Faculty of Science, Kyoto Sangyo University, Kyoto 603-8555, Japan

¹⁷Livision of physics, Mathematics, and Astronomy, California institute of Technology, Pasadena, CA 91125, USA

¹⁸Department of Physics, University of Warwick, Gibbet Hill Road, Coventry, CV4 7AL, UK

(Revised December 28, 2021; Accepted December 28, 2021)

Submitted to Astronomical Journal

ABSTRACT

We report the discovery of a sub-Jovian-mass planet, OGLE-2014-BLG-0319Lb. The characteristics of this planet will be added into a future extended statistical analysis of the Microlensing Observations in Astrophysics (MOA) collaboration. The planetary anomaly of the light curve is characterized by MOA and OGLE survey observations and results in three degenerate models with different planetary mass-ratios of $q = (10.3, 6.6, 4.5) \times 10^{-4}$, respectively. We find that the last two models require unreasonably small lens-source relative proper motions of $\mu_{\text{rel}} \sim 1 \text{ mas/yr}$. Considering Galactic prior probabilities, we rule out these two models from the final result. We conduct a Bayesian analysis to estimate physical properties of the lens system using a Galactic model and find that the lens

system is composed of a $0.49^{+0.35}_{-0.27} M_{\text{Jup}}$ sub-Jovian planet orbiting a $0.47^{+0.33}_{-0.25} M_{\odot}$ M-dwarf near the Galactic bulge. This analysis demonstrates that Galactic priors are useful to resolve this type of model degeneracy. This is important for estimating the mass ratio function statistically. However, this method would be unlikely successful in shorter timescale events, which are mostly due to low-mass objects, like brown dwarfs or free-floating planets. Therefore, careful treatment is needed for estimating the mass ratio function of the companions around such low-mass hosts which only the microlensing can probe.

1. INTRODUCTION

To date, more than 4000 exoplanets have been discovered (Akeson et al. 2013), revealing the universality and the diversity of planetary systems. Most of the known planets were discovered by the transit (Charbonneau et al. 2000) and the radial-velocity (RV; Butler et al. 2006) methods that are relatively sensitive to planets massive and close to their host stars, and thus the distribution of close-orbit exoplanets within ~ 1 au have been revealed in detail by these methods (e.g., Marcy et al. 2005; Cumming et al. 2008; Howard et al. 2012; Fressin et al. 2013). On the other hand, gravitational microlensing has a unique sensitivity to wide-orbit planets down to an Earth mass (Gould & Loeb 1992; Bennett & Rhee 1996) beyond the snow line where planet formation is considered to be the most efficient in the core accretion model (Lissauer 1993). This sensitivity is complementary to that of other detection methods.

The most recent statistical analysis using the largest sample of microlensing planets was conducted by Suzuki et al. (2016), who studied six years of survey data from the second phase of the Microlensing Observations in Astrophysics (MOA-II; Bond et al. 2001; Sumi et al. 2003) collaboration, including 23 planets discovered from 1474 microlensing events in 2007-2012. They find that the planet-frequency function in the power law describing planet/host mass-ratio q has a break around $q \sim 2 \times 10^{-4}$, which implies Neptune-mass-ratio planets are the most abundant type of planet beyond the snow line. Moreover, Suzuki et al. (2018) compared the mass-ratio function with planet population synthesis models (Ida & Lin 2004) and found a discrepancy over the range $10^{-3} < q < 4 \times 10^{-3}$ of a factor of ~ 10 , suggesting there is no desert of sub-Saturn-mass planets beyond the snow line. This is contrary to the prediction from the runaway accretion process in the core accretion model (e.g., Pollack et al. 1996). This result is also recently confirmed by the CORALIE/HARPS sample of planets found by the RV method (Bennett et al. 2021). These comparisons between observations and theories can provide op-

portunities to quantitatively diagnose sources of problems in calculation or theory (Suzuki et al. 2018). The MOA collaboration is planning to present new results of a statistical analysis using the extended sample of Suzuki et al. (2016) including ~ 50 planets detected by the MOA-II survey (D. Suzuki et al. in prep.). OGLE-2014-BLG-0319Lb which is detailed in this paper will be entered into this statistical sample.

In general, planetary signals in microlensing events appear as short-lived anomalous deviations from typical single-lens light curves (Paczynski 1986; Mao & Paczynski 1991) and sometimes produce a degeneracy problem where several model interpretations are possible for an anomaly. The origins of the degeneracy in microlensing events are summarized in detail in Han et al. (2018). Identifying all possible models and degeneracies for each planetary event is important for the completeness of a statistical microlensing analysis because systematic analysis with automated parameter searches can sometimes miss the best-fit models for each events (e.g., OGLE-2013-BLG-0911; Shvartzvald et al. 2016; Miyazaki et al. 2020). Furthermore, investigating the origin of the degeneracy for each event would be important because this adds to the growing body of literature on this topic and thus helps avoid missing models in future analyses.

In this paper, we analyze a microlensing event OGLE-2014-BLG-0319 that presents three planetary interpretations of different mass ratios of $q = (10.3, 6.6, 4.5) \times 10^{-4}$ and investigate the origin of the model degeneracy. The structure of this paper is as follows. In Section 2, we describe the observation and the data sets of the event. We present our light curve analysis and discuss the degeneracy in Section 3. We estimate physical properties of the lens and source systems in Section 4 and finally summarize and discuss the result in Section 5.

2. OBSERVATIONS & DATA REDUCTIONS

The microlensing event OGLE-2014-BLG-0319 occurred at $(\alpha, \delta)_{\text{J2000}} = (17:47:50.68, -33:56:06.16)$ which corresponds to $(l, b) = (-4.0306, -2.9971)$ in Galactic coordinates. The fourth phase of the Optical Gravitational Lensing Experiment (OGLE-IV; Udalski et al. 2015) collaboration firstly discovered and reported the

* MOA collaboration

† OGLE collaboration

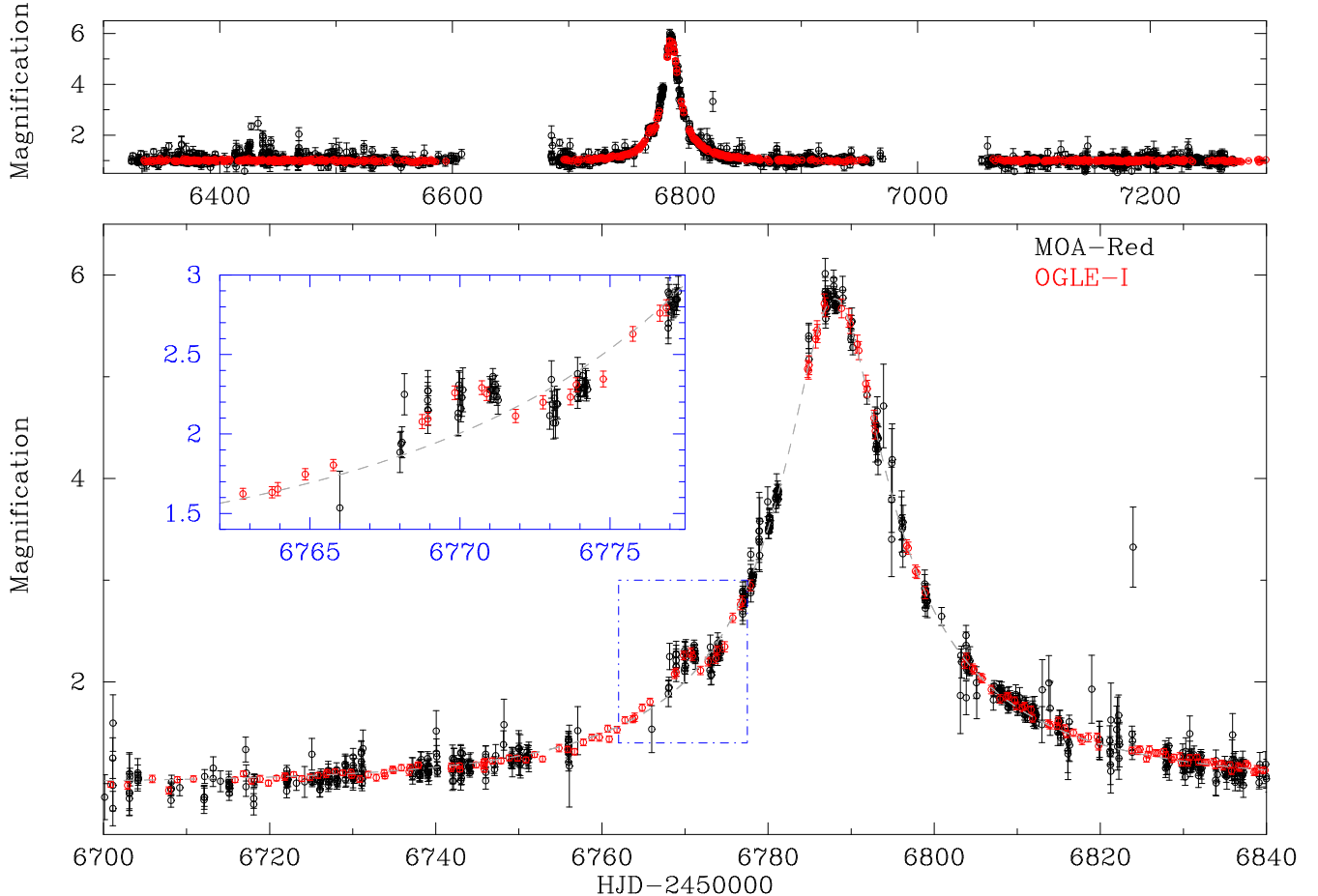


Figure 1. Light curve of OGLE-2014-BLG-0319 from the OGLE (red points) and MOA (black points) data. The gray dashed lines in panels represent the best-fit single-lens model. The blue panel shows a zoom-in view corresponding to the area surrounded by a blue chain line.

event on 2014 March 21 (about 50 days before the peak) through their Early Warning System (Udalski 2003). The OGLE field (BLG603) in which the event occurred was observed at a cadence of once per night by their 1.3m Warsaw telescope at Las Campanas Observatory in Chile using the OGLE-IV camera which has a 1.4 deg^2 field of view (FOV). OGLE uses the standard Kron-Cousins *I*-band filter in their regular surveys. They also use the *V*-band filter in their occasional observations in order to mainly measure source star color. For this event, they did not conduct any *V*-band observations.

Independently, the second phase of Microlensing Observations in Astrophysics (MOA-II) collaboration identified and reported the event as MOA-2014-BLG-171. The MOA field (gb1) in which the event occurred was observed at a cadence of once per 45 minutes by their 1.8m MOA-II telescope at Mt. John Observatory in New Zealand using the MOA-cam3 camera which has a 2.2 deg^2 FOV (Sako et al. 2008). MOA uses in their regular survey observations a custom band-pass filter, named MOA-Red, which is similar to the sum of the standard

Kron-Cousins *I*- and *R*-band filters. They also occasionally conduct *V*-band observations, but they did not observe in the *V*-band when the source star was magnified.

The data reductions for the OGLE and MOA data were conducted using their photometry pipelines (Wozniak 2000; Bond et al. 2001) which are optimized in their implementations of the different image analysis (DIA; Alard & Lupton 1998) method. The OGLE photometry is calibrated to the standard Cousins *I*-band (Szymański et al. 2011). In the MOA data, we found significant systematic variations in the light curve that are likely to be correlated with the seeing and airmass values. We measured and corrected the systematic trends by running a detrending code (Bond et al. 2017), which yielded a χ^2 improvement of $\Delta\chi^2 \sim 0.3$ per data point in the baseline and thus significantly reduced the systematic trends in the MOA light curve. We ran several of our detrending codes as used in Koshimoto et al. (2017) and confirmed that these corrections are consistent with each

Table 1. Data Sets for OGLE-2014-BLG-0319

Label	Telescope	Passband	N_{data}^a	k^b	σ_{\min}^b
MOA	MOA-II 1.8m	MOA-Red	3147	1.891	0.003
OGLE	Warsaw 1.3m	I	724	1.306	0.013

^aThe number of the data points.

^bThe coefficients for the renormalization. See text.

other. We also confirmed that this detrending procedure hardly affects the best-fit parameters for this event.

In general, for crowded stellar regions toward the Galactic bulge, the error bars derived by each photometry pipeline are underestimated (or overestimated), which can lead to incorrect conclusions and uncertainties on physical parameters. In order to correct this, we renormalize the error bars by $\sigma'_i = k\sqrt{\sigma_i^2 + e_{\min}^2}$, where σ_i and σ'_i are the original and corrected error bars in magnitude respectively, and k and e_{\min} are renormalization coefficients (Bennett et al. 2008; Yee et al. 2012). We select k and e_{\min} to satisfy $\chi^2/\text{dof}=1$ for each data set and make the cumulative χ^2 distribution sorted by the source magnification as uniform a cumulative distribution as possible. We first find a preliminary best-fit model using the original light curves. Next, we renormalize the error bars applying k and e_{\min} values to satisfy the conditions referred above. Finally, we find the final best-fit model fitting all the renormalized light curves. We note that the best-fit model parameters and the final results are not sensitive to moderate changes of the renormalization factors (Ranc et al. 2019). The data sets and the renormalization coefficients used in our analysis are summarized in Table 1.

Figure 1 shows the light curve from the OGLE and MOA data for OGLE-2014-BLG-0319. Prior to the peak of the event, a significant deviation of the light curve from a standard single-lens single-source (1L1S; Paczynski 1986) model was observed around $\text{HJD}' = 6772^1$. The anomaly was not noticed in real-time and was first announced on 2014 April 30 ($\text{HJD}' = 6778$) when the deviation almost finished so that any follow-up observations were not conducted during the anomaly. However, the deviation lasted about 10 days and both the OGLE and MOA regular observations could measure the deviation. After that, some modelers in survey groups immediately performed binary-lens modeling for this event

¹ $\text{HJD}' = \text{HJD} - 2450000$.

using the light curves produced by their real-time photometry pipelines which returns relatively rough DIA photometry^{2,3}. D. P. Bennett, one of the modelers, suggested in their private communication on 2014 May 17 that the anomaly could be explained with planetary-mass-ratio models although there is a potential model degeneracy, i.e. several competing models exist.

3. LIGHT-CURVE MODELING

As shown in Figure 1, the light curve of OGLE-2014-BLG-0319 shows a significant deviation from a Paczynski (1986) single-lens single-source (1L1S) model. Such a deviation could be produced by a single-lens binary-source (1L2S) model (Gaudi 1998; Shin et al. 2019). However, we find that this 1L2S scenario is not preferred by $\Delta\chi^2 > 170$ comparing with the best-fit binary-lens single-source (2L1S) model⁴. The anomaly comprises of the bump and dip parts deviating from the 1L1S model, and is well-separated from the peak of the light curve, which implies the anomaly is likely due to the source crossing over or near planetary caustics.

Here we present an exploration of the best-fit model to explain the nature of OGLE-2014-BLG-0319. Our light-curve modeling is done by our implementations of the image centered ray-shooting method (Bennett & Rieh 1996; Bennett 2010) and the Markov Chain Monte Carlo (MCMC) technique (Verde et al. 2003). In our analysis, we use a linear limb-darkening model for the source star. We apply the linear limb-darkening coefficients as $u_I = 0.5880$ and $u_{\text{MOA-Red}} = 0.63445$, which are based on the extinction-corrected source color described in Section 4.1 and the ATLAS model (Claret & Bloemen 2011).

3.1. Heuristic Analysis

We first present a heuristic analysis to predict the binary-lens parameters that produce the anomaly (Gould & Loeb 1992; Hwang et al. 2018; Skowron et al. 2018). This analysis is useful for discussing the origin of the model degeneracy for this event. The 1L1S modeling yields the parameters $(t_0, t_{\text{eff}}, t_E) \sim (6788.0, 6.0, 35.9)$ days, where t_0 is the time when the source approaching closest to the lens, t_E is the Einstein radius crossing time, $t_{\text{eff}} (\equiv u_0 t_E)$ is the effective event timescale, and u_0 is the impact parameter in unit of the angular Einstein radius θ_E . From Figure 1, the perturbation is centered at $t_{\text{anom}} \sim 6770.0$ and then $\tau_{\text{anom}} \equiv (t_0 - t_{\text{anom}})/t_E \sim$

² MOA, <http://www.massey.ac.nz/~abond/mao/alerts/>

³ OGLE, <http://ogle.astrouw.edu.pl/ogle4/ews/ews.html>

⁴ The χ^2 differences between the 2L1S and 1L1S models are ~ 340 for all the data and ~ 220 only for the MOA data.

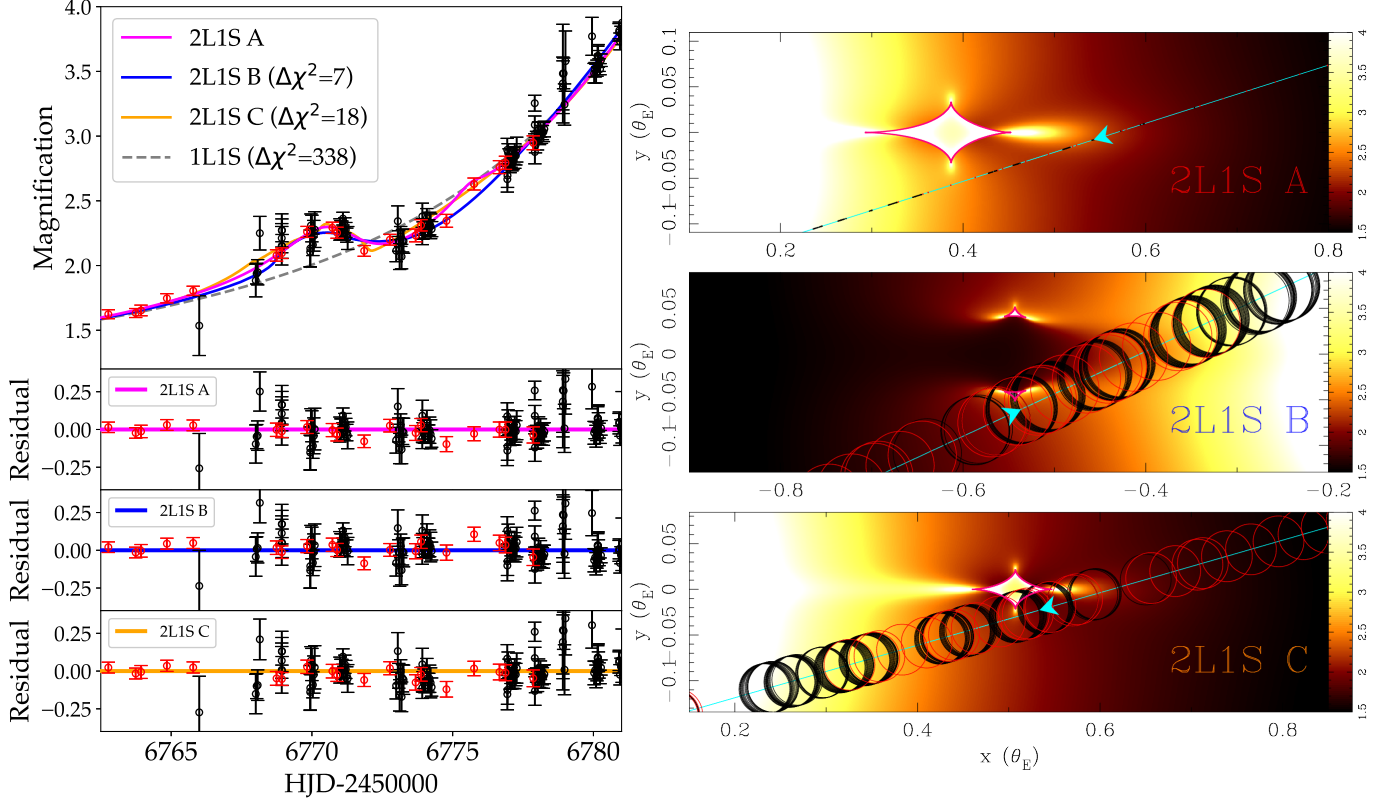


Figure 2. Comparison of the three local solutions, models A, B, and C. **(left panel)** The left panel shows a detailed view of the light curves when the anomaly occurred. Each 2L1S model curve is presented by colored solid lines and the 1L1S model curve is shown as a dashed gray line. The black and red circles with error bars are the light curves of MOA and OGLE, respectively. **(right panel)** The right three panels show the geometries of planetary caustics (magenta solid lines) relative to the source trajectories (cyan solid lines) for each model. The cyan arrows indicate the directions in which the sources are moving. The black and red circles represent the source positions when the MOA and OGLE measurements were conducted. The sizes of the circles are the best-fit source size of each model. The magnification maps are represented as color maps in each panel.

0.45. Therefore, if the perturbation is induced by a planet, the source position at the anomaly u_{anom} and the angle between the source trajectory and the binary-axis α (Rattenbury et al. 2002) would be

$$u_{\text{anom}} = \sqrt{u_0^2 + \tau_{\text{anom}}^2} \sim 0.53$$

$$\alpha = \tan^{-1} \left(\frac{u_0}{\tau_{\text{anom}}} \right) \sim 18.3^\circ.$$

The projected separation between the lens host and planet in unit of θ_E , s , can be estimated by $s - s^{-1} = u_{\text{anom}}$ and then we approximately estimate $s \sim 0.77$ and 1.30. This estimation is based on the assumption that the perturbation was induced by the source directly crossing over the planetary caustics.

The remaining binary-lens parameters are (q, ρ) , where q is the planet/host mass ratio and ρ is the source angular radius in unit of θ_E . There are no sharp caustic-crossing features in the light curve so that we expect two cases that (1) the source directly passes over the planetary caustic and then fully or partially envelops the

caustic (i.e. $q/\rho^2 \leq 1$) and (2) the source passes near the caustic. Here, we consider the case 1 and then estimate $\rho \simeq t_{\text{bump}}/2t_E = 0.04$, where $t_{\text{bump}} = 3$ days is the duration of the first bump in the anomaly. Under assumptions that the source is much larger than the Einstein radius of the planet $\theta_{E,p} (\equiv \sqrt{q}\theta_E)$ and $s > 1$, the maximum excess magnification is $\Delta A = 2q/\rho^2$ (Gould & Gaucherel 1997). In this case, we estimate $q \sim 3 \times 10^{-4}$, where $\Delta A = 0.3$. This result implies that the anomaly was caused by a sub-Jovian-mass-ratio planet.

The heuristic analysis presented above is incomplete because it is based on several assumptions and we do not consider the case in which the source does not directly cross over the caustic. In order to avoid missing any 2L1S solutions for the event, we conduct a detailed grid search analysis in the next section. However, as discussed in Section 3.3, this heuristic analysis would help us for understanding what is the origin of the model degeneracy that we will find.

3.2. Grid Search Analysis

In order to avoid missing any local 2L1S solutions for the event, we conducted a grid search over the (q, s, α) parameter space where these three parameters are known to strongly affect the magnification pattern. We set $40 \times 40 \times 60 = 96,000$ grid points distributed at equal intervals over the search ranges of $-6 \leq \log q \leq 0$, $-1 \leq \log s \leq 1$, and $0 \leq \alpha < 2\pi$, respectively, and then we ran MCMC samplers at each grid point allowing all the parameters to vary except for (q, s, α) . The initial parameters of (t_0, t_E, u_0) are randomly set to be within the uncertainties of the 1L1S model. The source radius crossing time, $t_* (= \rho t_E)$, is also an important parameter for the magnification pattern (e.g. [Bennett et al. 2008, 2014](#)) so that we randomly set an initial value of ρ at each grid point over $10^{-5} < \rho < 0.08$. After that, we refined all the possible models by allowing all the parameters to vary and then excluded models with $\Delta\chi^2 > 100$ compared to the best-fit model.

Our detailed grid search analysis found three different local minima for the 2L1S model. Here we label the three models in the ranked order of the χ^2 goodness-of-fit values as “model A”, “model B”, and “model C”. The model parameters and χ^2 values for each model are summarized in Table 2. Figure 2 allows a comparison between the three degenerate models. As shown in Figure 2, all the three models fit the light curve perturbation by the sources crossing near or over the planetary caustics, and model A is preferred over model B and C by $\Delta\chi^2 = 7.5$ and 18.4, respectively. We also tried to fit these models including high-order microlensing effects, parallax ([Gould 2004; Muraki et al. 2011](#)), xallarap ([Poindexter et al. 2005; Miyazaki et al. 2021](#)), and lens-orbital motion ([Skowron et al. 2011](#)). However, we found that these effects are not significant for this event and we could not obtain any meaningful constraints from the effects. This is probably because the effects are expected to be weak due to the relatively short timescale $t_E \sim 30$ days and large impact parameter $u_0 \sim 0.2$ ⁵.

3.3. Origin of the Degeneracy

Here we discuss the origin of the model degeneracy found in the previous section. In Section 3.1, we estimated $s \sim 0.77$ and 1.30 based on the assumption that the source directly crosses over the planetary caustic. Models B and C would enter into the group of models

⁵ Moreover, we found the baseline variability of the light curve remains even if we tried to remove it, which can systematically affect our secure measurements on the high-order effects. Therefore, we focus on the static models.

Table 2. Binary-lens Model Parameters

Parameters (Units)	Model A	Model B	Model C
t_0 (HJD' – 6780)	$7.963^{+0.025}_{-0.025}$	$8.035^{+0.024}_{-0.023}$	$8.045^{+0.024}_{-0.024}$
t_E (day)	$34.46^{+0.46}_{-0.47}$	$34.74^{+0.41}_{-0.43}$	$34.79^{+0.48}_{-0.45}$
u_0	$0.174^{+0.003}_{-0.003}$	$0.175^{+0.003}_{-0.003}$	$0.171^{+0.003}_{-0.003}$
q (10^{-4})	$10.34^{+1.31}_{-1.11}$	$6.56^{+0.61}_{-0.53}$	$4.51^{+0.87}_{-0.77}$
s	$1.213^{+0.005}_{-0.006}$	$0.762^{+0.003}_{-0.003}$	$1.287^{+0.005}_{-0.005}$
α (radian)	$2.834^{+0.003}_{-0.003}$	$5.845^{+0.006}_{-0.006}$	$2.859^{+0.005}_{-0.005}$
ρ (10^{-2})	$< 2.7^a$	$3.95^{+0.31}_{-0.26}$	$2.82^{+0.39}_{-0.34}$
t_* (day)	$< 0.78^a$	$1.37^{+0.10}_{-0.09}$	$0.98^{+0.13}_{-0.12}$
best-fit χ^2	3867.93	3875.41	3886.31
$\Delta\chi^2$	–	7.48	18.38

NOTE—Medians of the MCMC posterior distributions with uncertainties corresponding to the 68% credible intervals around the medians.

^a 3σ upper limits.

we predicted because of the fact that the source crossing over the caustic and the similarity of s . As expected, given there were no sharp caustic-crossing features in the anomaly, the source sizes for the both models are relatively large compared to the caustics, which is shown in the right panels of Figure 2, and the source sizes are well constrained. On the other hand, we found model A, with a significantly smaller source size, provides a somewhat better fit. This model can be considered as the case we did not consider in Section 3.1. In this case, the source crosses near the planetary caustic to reproduce the smooth perturbation. To illuminate this discussion, we introduce the parameter ([Hwang et al. 2018](#)),

$$|\Delta\xi| = |u_0 \csc \alpha' - \xi_{\pm}|, \quad (1)$$

where $\alpha' = \alpha \pm n\pi$ is defined to satisfy $\alpha' < \frac{\pi}{2}$ and $\xi_{\pm} = |s - s^{-1}|$. Hence $|\Delta\xi|$ approximately represents the distance between the center of the source and the caustic when the source crosses the binary-lens axis. Figure 3 represents the MCMC distribution colored by $\Delta\chi^2$ for each model on $(|\Delta\xi|, t_*)$, $(|\Delta\xi|, \log q)$, and $(\log s, \log q)$ planes. One sees that the three models seem continuous in the $(|\Delta\xi|, \log q)$ plane. However, model A is clearly separated from the model B and C on the $(|\Delta\xi|, t_*)$ plane and we note that the models B and C are well-separated on $(\log s, \log q)$ plane. Therefore, the three models are discrete on the microlensing parameter spaces and thus distinguishable. Although the model degeneracy for the event is within our expectations from the heuristic analysis and the visual inspection of the light curve, the degeneracy is worth discussing.

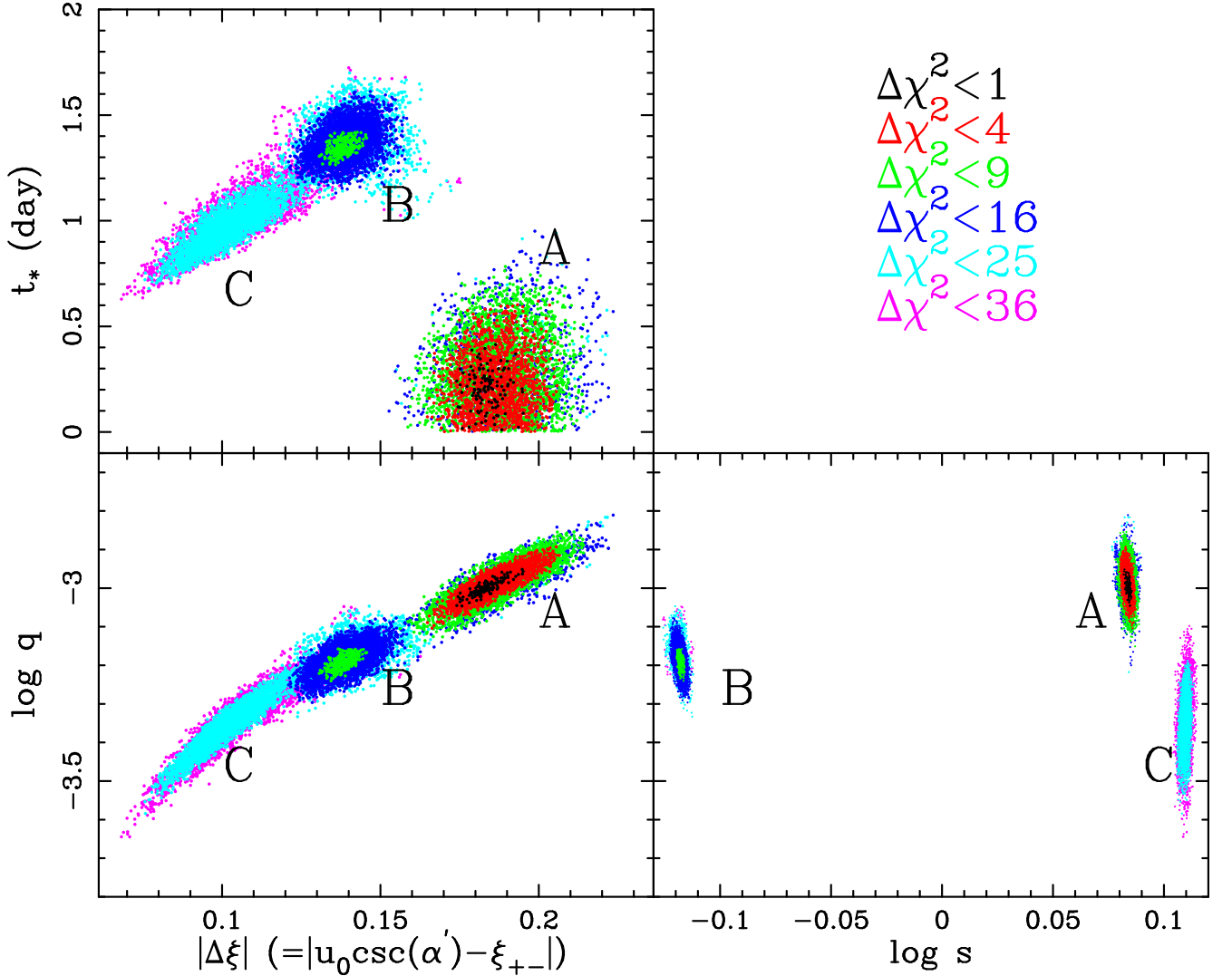


Figure 3. The $\Delta\chi^2$ distribution in the MCMC chains on $(|\Delta\xi|, t_*)$, $(|\Delta\xi|, \log q)$, and $(\log s, \log q)$ planes for each model, where the points of black, red, green, blue, cyan, and magenta represent the MCMC links with $\Delta\chi^2 < (1, 4, 9, 16, 25, 36)$, respectively.

A first degeneracy is between models with $s > 1$ and $s < 1$ at planetary caustic perturbations, i.e. the degeneracy between models B and C for this event. In general, the degeneracy could be resolvable because the caustic structures between them are qualitatively quite different and the light-curve features and the timing of the anomalies are different enough to distinguish them. The reason why the degeneracy occurred in this event would be due to the large source radii that “wash out” the magnification patterns and then the both models reproduce similar magnification patterns. Gaudi & Gould (1997) also predict such a degeneracy, see their Figure 1. Recently, Zang et al. (2021a) also encountered the similar degeneracy in a planetary event with $q \sim 10^{-5}$ and $\rho \sim 10^{-3}$. A second degeneracy is between models with sources crossing near the caustic and models with large sources crossing over the caustic, i.e. the degeneracy be-

tween models A and C for this event. This degeneracy was also found in Zang et al. (2020). In this degeneracy, one can constrain the source size which is relatively large compared with the caustic and the other can not, which is also demonstrated in Zang et al. (2020). This is qualitatively possible for planetary-caustic events with no sharp caustic-crossing features.

4. PHYSICAL PROPERTIES

The angular Einstein radius θ_E provides the important mass-distance relation for the lens system:

$$M_L = \frac{c^2}{4G} \theta_E^2 \frac{D_S D_L}{D_S - D_L}, \quad (2)$$

where D_S and D_L are the distances of the source and the lens from the observer, respectively. In order to determine θ_E , we measure the angular source radius

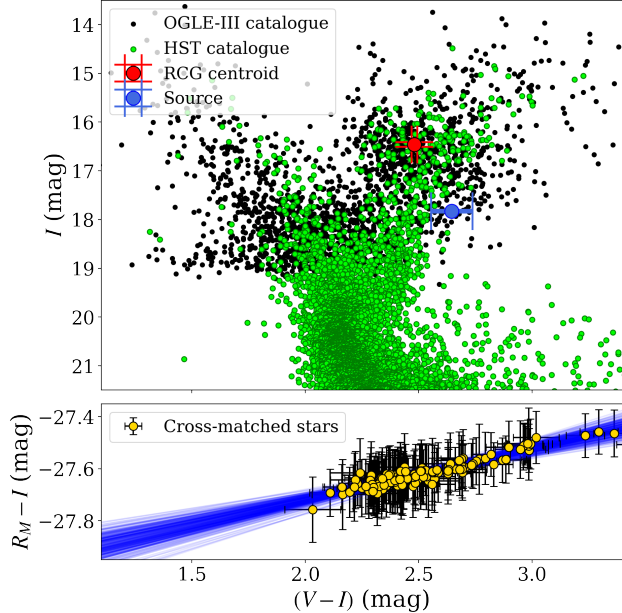


Figure 4. (Top panel): The $(V - I, I)$ color magnitude diagram (CMD) in the standard Kron-Cousins I and Johnson V photometric system. The positions of the Red Clump (RC) centroid and the source are presented as the red and blue circles. The black dots indicate stars of the OGLE-III catalogue within $2'$ of the event. The green circles indicate the *Hubble Space Telescope* (*HST*) catalogue (Holtzman et al. 1998) whose position is matched using the RC centroid. (Lower panel): The empirical color-color relation between the standard system $(V - I)$ and instrumental color $(R_{MO} - I)$. The blue translucent lines is 300 samples randomly extracted from the MCMC distribution.

θ_* ($\equiv \rho\theta_E$) which can be estimated from its color and magnitude (Boyajian et al. 2014).

4.1. Source Property

As mentioned in Section 2, we do not have any measurements in the V -band for this event. The source magnitudes in the I -band (I_S) and the MOA-Red band ($R_{M,S}$) are precisely measured from the light curve analysis and these enable us to estimate the source color of $(V - I)$ using an empirical color-color relation between $(R_M - I)$ and $(V - I)$ (Gould et al. 2010; Bennett et al. 2012). We note that the MOA light curve is scaled to match the instrumental MOA-II DOPHOT catalog (Bond et al. 2017) and the OGLE light curve is calibrated to the standard Cousins I -band.

We extracted isolated and relatively-bright stars in the OGLE-III catalog which are located within a $2'$ circle centered on the event and then cross-referenced the stars in the MOA-II catalog. We removed stars with colors $(V - I) < 2.0$ and then derived the following relation using an MCMC algorithm with 144 cross-matched

stars:

$$R_M - I = (0.196_{-0.027}^{+0.026})(V - I) - 28.112_{-0.068}^{+0.067},$$

where the parameter uncertainties for the slope and intercept correspond to the 1 sigma credible intervals around the median values in the MCMC stationary distribution. In the bottom panel of Figure 4, we show 300 relations (blue translucent lines) randomly extracted from the MCMC distribution. There is a strong correlation between the slope and intercept parameters in the MCMC distribution. Using the color-color relation, we estimated the source color and magnitude to be $(V - I, I)_S = (2.643, 17.829) \pm (0.046, 0.004)$ for model A. We note that the uncertainty of the source color $(V - I)_S$ largely comes from the uncertainty of the color-color relation.

Figure 4 also shows the $(V - I, I)$ color-magnitude diagram (CMD) of the OGLE-III catalog within $2'$ of the event which is calibrated to the standard photometric system (Szymański et al. 2011). We also plot the CMD of the *Hubble Space Telescope* (*HST*) catalogue (Holtzman et al. 1998) and found that the source color is somewhat redder than a sub-giant group in the Galactic bulge. We estimated the average color of the sub-giant group in the *HST* CMD following Bennett et al. (2008) as $(V - I)_{HST} = 2.43 \pm 0.11$ and confirmed that this is consistent with $(V - I)_S$ at 2σ . To be consistent with each color, we doubled the nominal error bars on the source color and thus adopted $(V - I)_S = 2.643 \pm 0.093$ in later analysis. Then, we estimated the position of the RC centroid in the CMD to be $(V - I, I)_{RC} = (2.481, 16.464) \pm (0.013, 0.050)$. Comparing $(V - I, I)_{RC}$ with the intrinsic RC color and magnitude $(V - I, I)_{RC,0} = (1.060, 14.605) \pm (0.060, 0.040)$ (Bensby et al. 2013; Nataf et al. 2013), we estimated the RC reddening and extinction to be $E(V - I)_{RC} = 1.421 \pm 0.061$ and $A_{I,RC} = 1.856 \pm 0.064$, respectively, and then derived the extinction-corrected source color and magnitude $(V - I, I)_{S,0} = (1.223, 15.973) \pm (0.111, 0.064)$ on the assumption that the source suffers the same extinction as the RC in the bulge (Yoo et al. 2004).

Using the intrinsic source color and magnitude and the following empirical relation (Boyajian et al. 2014):

$$\log(2\theta_*/\text{mas}) = 0.5014 + 0.4197(V - I)_{S,0} - 0.2I_{S,0},$$

we derived the angular source radius $\theta_* = 3.303 \pm 0.374 \mu\text{as}$ for model A. We summarize the source properties for each model in Table 3.

4.2. Angular Einstein Radius

Table 3. Source Properties

	Model A	Model B	Model C
$(V - I)_S^a$	2.643 ± 0.093	2.675 ± 0.096	2.648 ± 0.093
I_S	17.829 ± 0.004	17.846 ± 0.004	17.868 ± 0.004
$(V - I)_{S,0}$	1.223 ± 0.111	1.254 ± 0.114	1.228 ± 0.111
$I_{S,0}$	15.973 ± 0.064	15.990 ± 0.064	16.012 ± 0.064
θ_* (mas)	3.303 ± 0.374	3.378 ± 0.390	3.261 ± 0.370

^aThe error bars are extended to be consistent with the average color of a sub-giant group in the *HST* CMD.

NOTE— $(V - I)_S$: apparent color; I_S : apparent magnitude; $(V - I)_{S,0}$: extinction-free color; $I_{S,0}$: extinction-free magnitude; θ_* : angular radius.

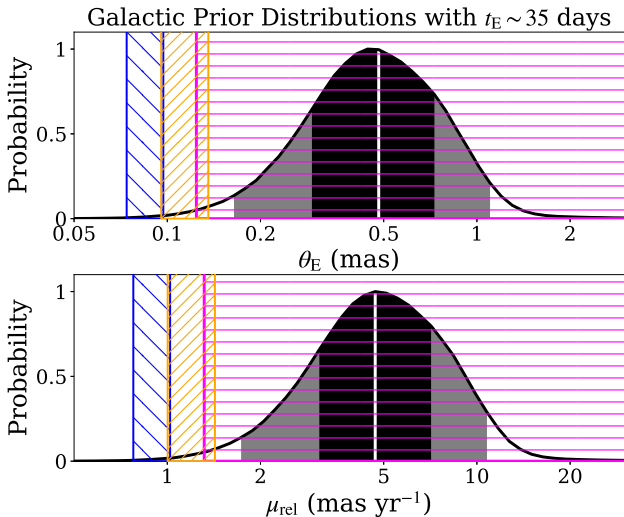


Figure 5. Prior probabilities of θ_E and μ_{rel} derived from a standard Galactic model, where the black and gray regions indicate the 68.3% (1 σ) and 95.4% (2 σ) credible intervals and the vertical white lines indicate the median values. Here the prior probabilities are weighted by the observed probability distribution of $t_E \sim 35$ day. The hatched region colored in magenta represents the 3 σ region for model A. And also, the regions colored in blue and orange represent the 1 σ regions for models B and C, respectively. The measured θ_E and μ_{rel} for models B and C are unreasonably small compared with the prior probabilities.

Finally, we estimate the angular Einstein radius θ_E ($\equiv \theta_*/\rho$) and the lens-source relative proper motion μ_{rel} ($\equiv \theta_E/t_E$) to be

$$\theta_E/(\text{mas}) = \begin{cases} > 0.124 & \text{(for Model A)} \\ 0.086 \pm 0.012 & \text{(for Model B)} \\ 0.116 \pm 0.020 & \text{(for Model C)} \end{cases}$$

and

$$\mu_{\text{rel}}/(\text{mas/yr}) = \begin{cases} > 1.316 & \text{(for Model A)} \\ 0.90 \pm 0.12 & \text{(for Model B)} \\ 1.21 \pm 0.21 & \text{(for Model C)} \end{cases}$$

respectively. We note that the limit for model A is the 3 sigma.

These observed angular Einstein radii for each model provide important constraints on the lens mass M_L and relative lens-source parallax $\pi_{\text{rel}} \equiv \text{au} (D_L^{-1} - D_S^{-1})$, as

$$M_L = \frac{\theta_E^2}{\kappa \pi_{\text{rel}}} = \begin{cases} > 0.063 \\ 0.030 \\ 0.055 \end{cases} M_{\odot} \left(\frac{0.03 \text{ mas}}{\pi_{\text{rel}}} \right), \quad (3)$$

where $\kappa = 8.144 \text{ mas}/M_{\odot}$ and $\pi_{\text{rel}} = 0.03 \text{ mas}$ is a typical value for lenses in the Galactic bulge. This implies that the lenses for models B and C would be sub-stellar objects, which is unlikely for microlensing events with $t_E \sim 35$ day (Sumi et al. 2011; Mróz et al. 2017). To quantitatively demonstrate this, we compared the observed θ_E and μ_{rel} values with prior probabilities derived from a Bayesian analysis using a Galactic model optimized for use in microlensing studies (Koshimoto et al. 2021a) detailed in the Section 4.3. Figure 5 shows the result and indicates that the observed θ_E and μ_{rel} values for models B and C are $\sim 3\sigma$ from the medians. Therefore, we conclude that models B and C are unlikely candidates for the best solution. This is in addition to the fact that they have worse χ^2 values⁶. We therefore conclude that model A is the best solution for the event. However, we should note that the prior probabilities presented in Figure 5 do not consider the planet-hosting probability that is likely dependent on properties of the host star, like mass, metallicity, and its Galactic location. A recent statistical study using 28 planetary events indicates that the dependence on the Galactic location might be small, however (Koshimoto et al. 2021b). For completeness, we summarize the final results of models B and C in Appendix A.

4.3. Bayesian Analysis

Because we can not obtain any significant parallax measurements, we can not directly determine the physical properties of the lens system. Therefore, we conducted a Bayesian analysis in order to quantitatively estimate the probability distribution of the physical properties. We employed a new parametric Galactic model

⁶ Under the assumption of a normal distribution, models B and C can be rejected at significant levels of ~ 0.02 and $\sim 10^{-4}$, respectively.

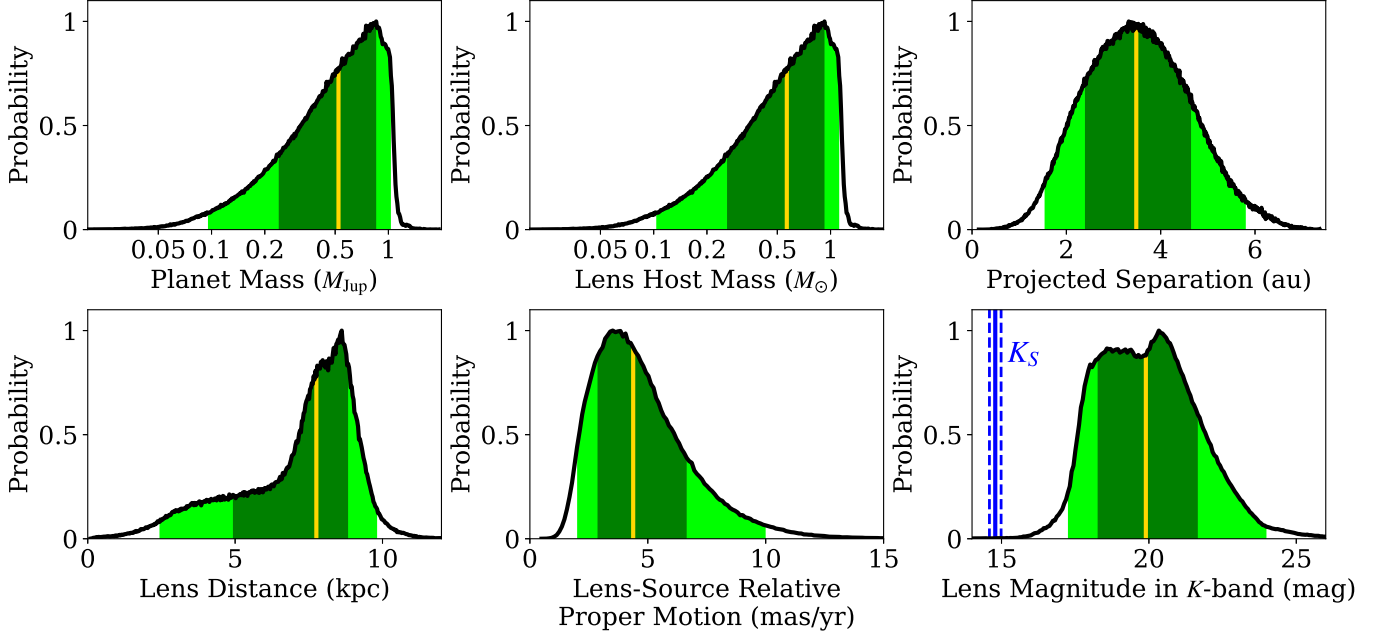


Figure 6. Posterior probability distributions of the physical parameters derived from a Bayesian analysis using a Galactic model. The green and light green regions indicate the 68.3% (1 σ) and 95.4% (2 σ) credible intervals and the vertical yellow lines indicate the median values. We also plot the expected source magnitude K_S in the lower right panel where the dashed lines indicate the 1 σ uncertainties.

Table 4. Physical Parameters

Physical Parameters (Units)	Median $\pm 1\sigma$
Planet Mass, M_P (M_{Jup})	$0.57^{+0.36}_{-0.31}$
Lens Host Mass, M_{Host} (M_{\odot})	$0.52^{+0.33}_{-0.29}$
Projected Semi-major Axis, a_{\perp} (au)	$3.49^{+1.17}_{-1.12}$
Distance to the Lens System, D_L (kpc)	$7.73^{+1.14}_{-2.84}$
Distance to the Source, D_S (kpc)	$10.30^{+3.35}_{-0.68}$
Angular Einstein Radius, θ_E (mas)	$0.41^{+0.22}_{-0.15}$
Lens-Source Proper Motion, μ_{rel} (mas/yr)	$4.38^{+2.32}_{-1.62}$
Lens Magnitude in I -band, I_L (mag)	$23.43^{+2.23}_{-2.26}$
Lens Magnitude in H -band, H_L (mag)	$20.29^{+1.86}_{-1.81}$
Lens Magnitude in K -band, K_L (mag)	$19.92^{+1.79}_{-1.70}$
Source Magnitude in H -band, H_S (mag)	15.04 ± 0.20
Source Magnitude in K -band, K_S (mag)	14.79 ± 0.20

developed to match recent various observation data toward the Galactic bulge. We generated $\sim 10^6$ artificial microlensing events using the public code `genulens`⁷ (Koshimoto & Ranc 2021). We then derived the posterior probability distribution weighting by the observed likelihood distributions of t_E , θ_E , I_S , and $(V - I)_S$. The result of the Bayesian analysis is shown in Figure 6 and

the physical parameters derived are summarized in Table 4. The analysis indicates that the lens system comprises of a sub-Jovian-mass planet orbiting an M-dwarf star near the Galactic bulge.

4.4. Future Follow-up Observation

Future follow-up observations with high-angular-resolution might be able to give an additional mass-distance relation derived from the lens flux. This can resolve the large uncertainties of the lens physical parameters (Bennett et al. 2015; Bhattacharya et al. 2018; Bennett et al. 2020; Bhattacharya et al. 2020; Vandorou et al. 2020; Terry et al. 2021). For this, we also estimate the apparent magnitude of the lens brightness in the Bayesian analysis. Here we model the extinction in front of the lens (Bennett et al. 2015) as

$$A_L = \frac{1 - e^{-D_L/(0.1\text{kpc}) \sin |b|}}{1 - e^{-D_S/(0.1\text{kpc}) \sin |b|}} A_S \quad (4)$$

where A_L and A_S are the extinction values for the lens and source systems, respectively. We used the mass-luminosity and color-color relations (Henry & McCarthy 1993; Kenyon & Hartmann 1995; Kroupa et al. 1993) and the extinction law (Nishiyama et al. 2009) to derive the apparent magnitudes of the lens and the source in different pass-bands. The result is summarized in Table 4. It is expected that the source is ~ 5.1 mag brighter than the lens in K -band and the angular separation between the source and the lens will be ~ 35 mas in 2022.

⁷ <https://github.com/nkoshimoto/genulens>

Owing to such a high contrast, several more years might need to pass in order to resolve the lens position and detect the lens flux. However, observing the lens not only can resolve the uncertainties of the physical parameters, it can also break the model degeneracy because each degenerate model indicates different lens-source relative proper motions μ_{rel} . Therefore, it would be worth conducting these future follow-up observations.

5. SUMMARY & DISCUSSION

We present the analysis of the planetary microlensing event OGLE-2014-BLG-0319. We find three possible models with different mass ratios $q = (10.3, 6.6, 4.5) \times 10^{-4}$ and lens-source relative proper motions $\mu_{\text{rel}} = (> 2.50, 0.90, 1.26)$ mas/yr, respectively. We rule out the last two models with small μ_{rel} values considering the Galactic prior probability. Finally, we conduct a Bayesian analysis using a Galactic model and estimate the lens system consists of a sub-Jupiter-mass planet orbiting an M-dwarf near the Galactic bulge.

5.1. Degeneracy of Mass Ratios and Proper Motions

In general, the mass-ratio q is approximately determined from the duration of planetary perturbation relative to t_E . If the source size is large relative to the Einstein radius of the planet, then the duration of the perturbation becomes the source crossing time. [Gaudi & Gould \(1997\)](#) predict a continuous degeneracy in such a case: $\mu_{\text{rel}}\rho q^{-1/2} = \text{const.}$ At a given μ_{rel} , the $q^{-1/2}$ and ρ can be degenerate. They also propose that the low-mass solutions with low μ_{rel} values could be *a priori* ruled out. For the event OGLE-2014-BLG-0319, we can rule out models B and C by comparing the measured values and the Galactic prior probabilities for θ_E and μ_{rel} . This approach can be made because the observed values are unlikely at a given $t_E \sim 35$ days⁸. However, we expect this would be more difficult for short-timescale (low-mass lens) events because $\rho \propto t_E^{-1}$ and $t_E \propto \sqrt{M_L}$. For example, a Bayesian analysis with $t_E \sim 5$ days provides high prior probabilities at $\theta_E \sim 0.1$ mas and $\mu_{\text{rel}} \sim 1$ mas/yr.

So far, there have been several reported short timescale events which suffered from similar model degeneracies between different q and μ_{rel} values (e.g., [Miyazaki et al. 2018](#); [Zhang et al. 2020](#)). These events have several degenerate solutions with $\rho \geq 0.01$ and $t_E \leq 10$ days and they can not be ruled out by Galactic

⁸ Interestingly, [Han et al. \(2020\)](#) reported a discovery of a planetary microlensing event with $t_E = 45$ days and $\mu_{\text{rel}} \sim 0.79$ mas/yr. Note that they confirmed that there are no competing models with the final result.

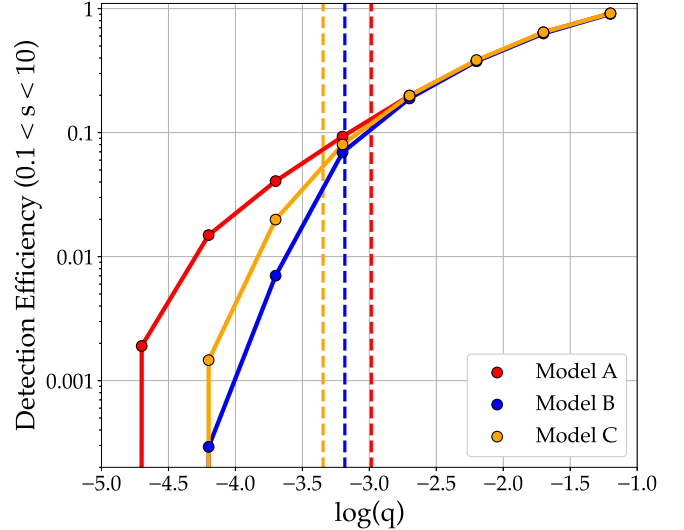


Figure 7. Detection efficiencies for each degenerate model as a function of mass-ratio q . The vertical dashed lines represents the observed q for each model. For model A, we used the best-fit value of $\rho = 7.0 \times 10^{-3}$ for calculation.

priors. As discussed in [Zhang et al. \(2020\)](#), the discovery rate of short timescale events with planetary (short-lived) perturbations has much increased since current second-generation microlensing surveys started. Hence, we can now explore planets around low-mass dwarfs, brown dwarfs, and even planetary-mass objects. However, the degeneracy would be more common for short timescale events and thus might have large impacts on the estimation for the frequency of such planets.

5.2. Detection Efficiency Dependent on Source Size

Furthermore, estimating different ρ values can lead to different detection efficiencies of planets for each event. Figure 7 shows the planet detection efficiencies for each model as a function of $\log q$, in which the dashed vertical lines represent the observed q for each model (Details of the calculation for the detection efficiency are similar with [Suzuki et al. 2016](#) and described in Section 4 of [Suzuki et al. 2016](#)). For this event, the different ρ estimation for each model does not strongly affect the efficiency at $\log q \sim -3$. However, the effect would be more serious at $\log q \ll -3$ where the detection efficiencies are different by an order of magnitude, as shown in Figure 7. This indicates that the detection efficiency of low mass-ratio planets around low-mass objects would largely be dependent on ρ ($\equiv \theta_*/\mu_{\text{rel}}t_E$) and calls our attention to some assumptions to estimate the detection efficiency. Recent planet discoveries with $q < 2 \times 10^{-5}$ have also shown that smaller ρ is more sensitive to low-mass planets; $\rho \sim 5 \times 10^{-4}$ (KMT-2018-BLG-0029, [Gould et al. 2020](#)), $\rho \sim 3 \times 10^{-4}$ (OGLE-2019-BLG-0960, [Yee et al.](#)

Table 5. Physical Parameters for Models B and C

Physical Parameters (Units)	Model B	Model C
Planet Mass, M_P (M_\oplus)	$17.05^{+25.71}_{-9.45}$	$17.14^{+24.35}_{-8.48}$
Lens Host Mass, M_{Host} (M_\odot)	$0.08^{+0.12}_{-0.04}$	$0.11^{+0.16}_{-0.06}$
Projected Semi-major Axis, a_\perp (au)	$0.64^{+0.10}_{-0.09}$	$1.45^{+0.27}_{-0.24}$
Distance to the Lens System, D_L (kpc)	$8.96^{+0.55}_{-0.63}$	$8.92^{+0.57}_{-0.71}$
Distance to the Source, D_S (kpc)	$10.12^{+1.85}_{-0.63}$	$10.29^{+1.67}_{-0.65}$
Angular Einstein Radius, θ_E (mas)	$0.10^{+0.01}_{-0.02}$	$0.13^{+0.02}_{-0.02}$
Lens-Source Proper Motion, μ_{rel} (mas/yr)	$0.97^{+0.12}_{-0.12}$	$1.32^{+0.20}_{-0.19}$
Lens Magnitude in I -band, I_L (mag)	$28.29^{+2.68}_{-2.12}$	$27.83^{+2.30}_{-2.04}$
Lens Magnitude in H -band, H_L (mag)	$26.61^{+6.16}_{-3.27}$	$24.51^{+5.89}_{-1.92}$
Lens Magnitude in K -band, K_L (mag)	$26.07^{+7.66}_{-3.21}$	$24.02^{+6.31}_{-1.89}$
Source Magnitude in H -band, H_S (mag)	15.04 ± 0.20	15.08 ± 0.20
Source Magnitude in K -band, K_S (mag)	14.78 ± 0.20	14.82 ± 0.20

2021), $\rho \sim 2 \times 10^{-3}$ (OGLE-2019-BLG-1053, Zang et al. 2021b), and $\rho \sim 6 \times 10^{-4}$ (KMT-2020-BLG-0414, Zang et al. 2021a).

For example, Suzuki et al. (2016) derived ρ values assuming that single-lens events have the similar μ_{rel} distribution to their planetary sample of $\mu_{\text{rel}} = 5.74^{+2.94}_{-2.84}$ mas yr $^{-1}$, and then calculated the detection efficiency for each event⁹. They demonstrated that the efficiency does not significantly depend on the derived ρ values within the 1σ uncertainties (See Figure 7 of Suzuki et al. 2016). Moreover, the μ_{rel} distribution they assumed is also consistent with the prediction of a Galactic model. However, it is unclear whether the assumption holds up in the low-mass regime because the Galactic model for low-mass objects like velocity distribution is still much less clear and might be different with those in stellar-mass regime (Sajadian et al. 2021). Considering the effect could be important to estimate the frequency of planets around low-mass dwarfs,

brown dwarfs (Lingam et al. 2020), and even moons around free-floating planets (Bennett et al. 2014). This would effectively be investigated by the Roman Galactic Exoplanet Survey (RGES; Penny et al. 2019; Johnson et al. 2020) which has much better sensitivity to short-timescale events than current microlensing surveys.

We would appreciate the anonymous referee for helping to improve the paper. We acknowledge the following support: Work by SM is supported by JSPS KAKENHI Grant Number 21J11296. The work of DPB., NK, CR, YH, and AB was supported by NASA under award number 80GSFC17M0002. CR is supported by the ANR project COLD-WORLDS of the French *Agence Nationale de la Recherche* with the reference ANR-18-CE31-0002. The MOA project is supported by JSPS KAKENHI grant No. 19KK0082 and 20H04754.

APPENDIX

A. PHYSICAL PARAMETERS FOR MODELS B AND C

For completeness, we present Table 5 that represents the physical parameters for models B and C, which is derived by the Bayesian analysis presented in Section 4.3.

⁹ Note that they calculated the detection efficiencies for each single-lens event using a value of $\mu_{\text{rel}} = 5.6$ mas/yr so that their final result does not include the uncertainties of μ_{rel} . However, they showed it hardly affects the final result.

REFERENCES

Akeson, R. L., Chen, X., Ciardi, D., et al. 2013, PASP, 125, 989, doi: [10.1086/672273](https://doi.org/10.1086/672273)

Alard, C., & Lupton, R. H. 1998, ApJ, 503, 325, doi: [10.1086/305984](https://doi.org/10.1086/305984)

Bennett, D. P. 2010, ApJ, 716, 1408, doi: [10.1088/0004-637X/716/2/1408](https://doi.org/10.1088/0004-637X/716/2/1408)

Bennett, D. P., Ranc, C., & Fernandes, R. B. 2021, arXiv e-prints, arXiv:2104.05713. <https://arxiv.org/abs/2104.05713>

Bennett, D. P., & Rhie, S. H. 1996, ApJ, 472, 660, doi: [10.1086/178096](https://doi.org/10.1086/178096)

Bennett, D. P., Bond, I. A., Udalski, A., et al. 2008, ApJ, 684, 663, doi: [10.1086/589940](https://doi.org/10.1086/589940)

Bennett, D. P., Sumi, T., Bond, I. A., et al. 2012, ApJ, 757, 119, doi: [10.1088/0004-637X/757/2/119](https://doi.org/10.1088/0004-637X/757/2/119)

Bennett, D. P., Batista, V., Bond, I. A., et al. 2014, ApJ, 785, 155, doi: [10.1088/0004-637X/785/2/155](https://doi.org/10.1088/0004-637X/785/2/155)

Bennett, D. P., Bhattacharya, A., Anderson, J., et al. 2015, ApJ, 808, 169, doi: [10.1088/0004-637X/808/2/169](https://doi.org/10.1088/0004-637X/808/2/169)

Bennett, D. P., Bhattacharya, A., Beaulieu, J.-P., et al. 2020, AJ, 159, 68, doi: [10.3847/1538-3881/ab6212](https://doi.org/10.3847/1538-3881/ab6212)

Bensby, T., Yee, J. C., Feltzing, S., et al. 2013, A&A, 549, A147, doi: [10.1051/0004-6361/201220678](https://doi.org/10.1051/0004-6361/201220678)

Bhattacharya, A., Beaulieu, J. P., Bennett, D. P., et al. 2018, AJ, 156, 289, doi: [10.3847/1538-3881/aaed46](https://doi.org/10.3847/1538-3881/aaed46)

Bhattacharya, A., Bennett, D. P., Beaulieu, J. P., et al. 2020, arXiv e-prints, arXiv:2009.02329. <https://arxiv.org/abs/2009.02329>

Bond, I. A., Abe, F., Dodd, R. J., et al. 2001, MNRAS, 327, 868, doi: [10.1046/j.1365-8711.2001.04776.x](https://doi.org/10.1046/j.1365-8711.2001.04776.x)

Bond, I. A., Bennett, D. P., Sumi, T., et al. 2017, MNRAS, 469, 2434, doi: [10.1093/mnras/stx1049](https://doi.org/10.1093/mnras/stx1049)

Boyajian, T. S., van Belle, G., & von Braun, K. 2014, AJ, 147, 47, doi: [10.1088/0004-6256/147/3/47](https://doi.org/10.1088/0004-6256/147/3/47)

Butler, R. P., Wright, J. T., Marcy, G. W., et al. 2006, ApJ, 646, 505, doi: [10.1086/504701](https://doi.org/10.1086/504701)

Charbonneau, D., Brown, T. M., Latham, D. W., & Mayor, M. 2000, ApJL, 529, L45, doi: [10.1086/312457](https://doi.org/10.1086/312457)

Claret, A., & Bloemen, S. 2011, A&A, 529, A75, doi: [10.1051/0004-6361/201116451](https://doi.org/10.1051/0004-6361/201116451)

Cumming, A., Butler, R. P., Marcy, G. W., et al. 2008, PASP, 120, 531, doi: [10.1086/588487](https://doi.org/10.1086/588487)

Fressin, F., Torres, G., Charbonneau, D., et al. 2013, ApJ, 766, 81, doi: [10.1088/0004-637X/766/2/81](https://doi.org/10.1088/0004-637X/766/2/81)

Gaudi, B. S. 1998, ApJ, 506, 533, doi: [10.1086/306256](https://doi.org/10.1086/306256)

Gaudi, B. S., & Gould, A. 1997, ApJ, 486, 85, doi: [10.1086/304491](https://doi.org/10.1086/304491)

Gould, A. 2004, ApJ, 606, 319, doi: [10.1086/382782](https://doi.org/10.1086/382782)

Gould, A., Dong, S., Bennett, D. P., et al. 2010, ApJ, 710, 1800, doi: [10.1088/0004-637X/710/2/1800](https://doi.org/10.1088/0004-637X/710/2/1800)

Gould, A., & Gaucherel, C. 1997, ApJ, 477, 580, doi: [10.1086/303751](https://doi.org/10.1086/303751)

Gould, A., & Loeb, A. 1992, ApJ, 396, 104, doi: [10.1086/171700](https://doi.org/10.1086/171700)

Gould, A., Ryu, Y.-H., Calchi Novati, S., et al. 2020, Journal of Korean Astronomical Society, 53, 9, doi: [10.5303/JKAS.2020.53.1.9](https://doi.org/10.5303/JKAS.2020.53.1.9)

Han, C., Bond, I. A., Gould, A., et al. 2018, AJ, 156, 226, doi: [10.3847/1538-3881/aae38e](https://doi.org/10.3847/1538-3881/aae38e)

Han, C., Udalski, A., Gould, A., et al. 2020, AJ, 159, 91, doi: [10.3847/1538-3881/ab6a9f](https://doi.org/10.3847/1538-3881/ab6a9f)

Henry, T. J., & McCarthy, Donald W., J. 1993, AJ, 106, 773, doi: [10.1086/116685](https://doi.org/10.1086/116685)

Holtzman, J. A., Watson, A. M., Baum, W. A., et al. 1998, AJ, 115, 1946, doi: [10.1086/300336](https://doi.org/10.1086/300336)

Howard, A. W., Marcy, G. W., Bryson, S. T., et al. 2012, ApJS, 201, 15, doi: [10.1088/0067-0049/201/2/15](https://doi.org/10.1088/0067-0049/201/2/15)

Hwang, K. H., Udalski, A., Shvartzvald, Y., et al. 2018, AJ, 155, 20, doi: [10.3847/1538-3881/aa992f](https://doi.org/10.3847/1538-3881/aa992f)

Ida, S., & Lin, D. N. C. 2004, ApJ, 604, 388, doi: [10.1086/381724](https://doi.org/10.1086/381724)

Johnson, S. A., Penny, M., Gaudi, B. S., et al. 2020, AJ, 160, 123, doi: [10.3847/1538-3881/aba75b](https://doi.org/10.3847/1538-3881/aba75b)

Kenyon, S. J., & Hartmann, L. 1995, ApJS, 101, 117, doi: [10.1086/192235](https://doi.org/10.1086/192235)

Koshimoto, N., Baba, J., & Bennett, D. P. 2021a, arXiv e-prints, arXiv:2104.03306. <https://arxiv.org/abs/2104.03306>

Koshimoto, N., Bennett, D. P., Suzuki, D., & Bond, I. A. 2021b, ApJL, 918, L8, doi: [10.3847/2041-8213/ac17ec](https://doi.org/10.3847/2041-8213/ac17ec)

Koshimoto, N., & Ranc, C. 2021, nkoshimoto/genulens: A Tool for Gravitational Microlensing Events Simulation, v1.0, Zenodo, doi: [10.5281/zenodo.4784949](https://doi.org/10.5281/zenodo.4784949)

Koshimoto, N., Udalski, A., Beaulieu, J. P., et al. 2017, AJ, 153, 1, doi: [10.3847/1538-3881/153/1/1](https://doi.org/10.3847/1538-3881/153/1/1)

Kroupa, P., Tout, C. A., & Gilmore, G. 1993, MNRAS, 262, 545, doi: [10.1093/mnras/262.3.545](https://doi.org/10.1093/mnras/262.3.545)

Lingam, M., Ginsburg, I., & Loeb, A. 2020, ApJ, 888, 102, doi: [10.3847/1538-4357/ab5b13](https://doi.org/10.3847/1538-4357/ab5b13)

Lissauer, J. J. 1993, ARA&A, 31, 129, doi: [10.1146/annurev.aa.31.090193.001021](https://doi.org/10.1146/annurev.aa.31.090193.001021)

Mao, S., & Paczynski, B. 1991, ApJL, 374, L37, doi: [10.1086/186066](https://doi.org/10.1086/186066)

Marcy, G., Butler, R. P., Fischer, D., et al. 2005, Progress of Theoretical Physics Supplement, 158, 24, doi: [10.1143/PTPS.158.24](https://doi.org/10.1143/PTPS.158.24)

Miyazaki, S., Johnson, S. A., Sumi, T., et al. 2021, AJ, 161, 84, doi: [10.3847/1538-3881/abcec2](https://doi.org/10.3847/1538-3881/abcec2)

Miyazaki, S., Sumi, T., Bennett, D. P., et al. 2018, AJ, 156, 136, doi: [10.3847/1538-3881/aad5ee](https://doi.org/10.3847/1538-3881/aad5ee)

—. 2020, AJ, 159, 76, doi: [10.3847/1538-3881/ab64de](https://doi.org/10.3847/1538-3881/ab64de)

Mróz, P., Udalski, A., Skowron, J., et al. 2017, Nature, 548, 183, doi: [10.1038/nature23276](https://doi.org/10.1038/nature23276)

Muraki, Y., Han, C., Bennett, D. P., et al. 2011, ApJ, 741, 22, doi: [10.1088/0004-637X/741/1/22](https://doi.org/10.1088/0004-637X/741/1/22)

Nataf, D. M., Gould, A., Fouqué, P., et al. 2013, ApJ, 769, 88, doi: [10.1088/0004-637X/769/2/88](https://doi.org/10.1088/0004-637X/769/2/88)

Nishiyama, S., Tamura, M., Hatano, H., et al. 2009, ApJ, 696, 1407, doi: [10.1088/0004-637X/696/2/1407](https://doi.org/10.1088/0004-637X/696/2/1407)

Paczynski, B. 1986, ApJ, 304, 1, doi: [10.1086/164140](https://doi.org/10.1086/164140)

Penny, M. T., Gaudi, B. S., Kerins, E., et al. 2019, ApJS, 241, 3, doi: [10.3847/1538-4365/aafb69](https://doi.org/10.3847/1538-4365/aafb69)

Poindexter, S., Afonso, C., Bennett, D. P., et al. 2005, ApJ, 633, 914, doi: [10.1086/468182](https://doi.org/10.1086/468182)

Pollack, J. B., Hubickyj, O., Bodenheimer, P., et al. 1996, Icarus, 124, 62, doi: [10.1006/icar.1996.0190](https://doi.org/10.1006/icar.1996.0190)

Ranc, C., Bennett, D. P., Hirao, Y., et al. 2019, AJ, 157, 232, doi: [10.3847/1538-3881/ab141b](https://doi.org/10.3847/1538-3881/ab141b)

Rattenbury, N. J., Bond, I. A., Skuljan, J., & Yock, P. C. M. 2002, MNRAS, 335, 159, doi: [10.1046/j.1365-8711.2002.05607.x](https://doi.org/10.1046/j.1365-8711.2002.05607.x)

Sajadian, S., Rahvar, S., & Kazemian, F. 2021, arXiv e-prints, arXiv:2103.10593. <https://arxiv.org/abs/2103.10593>

Sako, T., Sekiguchi, T., Sasaki, M., et al. 2008, Experimental Astronomy, 22, 51, doi: [10.1007/s10686-007-9082-5](https://doi.org/10.1007/s10686-007-9082-5)

Shin, I. G., Yee, J. C., Gould, A., et al. 2019, AJ, 158, 199, doi: [10.3847/1538-3881/ab46a5](https://doi.org/10.3847/1538-3881/ab46a5)

Shvartzvald, Y., Maoz, D., Udalski, A., et al. 2016, MNRAS, 457, 4089, doi: [10.1093/mnras/stw191](https://doi.org/10.1093/mnras/stw191)

Skowron, J., Udalski, A., Gould, A., et al. 2011, ApJ, 738, 87, doi: [10.1088/0004-637X/738/1/87](https://doi.org/10.1088/0004-637X/738/1/87)

Skowron, J., Ryu, Y. H., Hwang, K. H., et al. 2018, AcA, 68, 43, doi: [10.32023/0001-5237/68.1.2](https://doi.org/10.32023/0001-5237/68.1.2)

Sumi, T., Abe, F., Bond, I. A., et al. 2003, ApJ, 591, 204, doi: [10.1086/375212](https://doi.org/10.1086/375212)

Sumi, T., Kamiya, K., Bennett, D. P., et al. 2011, Nature, 473, 349, doi: [10.1038/nature10092](https://doi.org/10.1038/nature10092)

Suzuki, D., Bennett, D. P., Sumi, T., et al. 2016, ApJ, 833, 145, doi: [10.3847/1538-4357/833/2/145](https://doi.org/10.3847/1538-4357/833/2/145)

Suzuki, D., Bennett, D. P., Ida, S., et al. 2018, ApJL, 869, L34, doi: [10.3847/2041-8213/aaf577](https://doi.org/10.3847/2041-8213/aaf577)

Szymański, M. K., Udalski, A., Soszyński, I., et al. 2011, AcA, 61, 83. <https://arxiv.org/abs/1107.4008>

Terry, S. K., Bhattacharya, A., Bennett, D. P., et al. 2021, AJ, 161, 54, doi: [10.3847/1538-3881/abcc60](https://doi.org/10.3847/1538-3881/abcc60)

Udalski, A. 2003, AcA, 53, 291. <https://arxiv.org/abs/astro-ph/0401123>

Udalski, A., Szymański, M. K., & Szymański, G. 2015, AcA, 65, 1. <https://arxiv.org/abs/1504.05966>

Vandorou, A., Bennett, D. P., Beaulieu, J.-P., et al. 2020, AJ, 160, 121, doi: [10.3847/1538-3881/aba2d3](https://doi.org/10.3847/1538-3881/aba2d3)

Verde, L., Peiris, H. V., Spergel, D. N., et al. 2003, ApJS, 148, 195, doi: [10.1086/377335](https://doi.org/10.1086/377335)

Wozniak, P. R. 2000, AcA, 50, 421. <https://arxiv.org/abs/astro-ph/0012143>

Yee, J. C., Shvartzvald, Y., Gal-Yam, A., et al. 2012, ApJ, 755, 102, doi: [10.1088/0004-637X/755/2/102](https://doi.org/10.1088/0004-637X/755/2/102)

Yee, J. C., Zang, W., Udalski, A., et al. 2021, AJ, 162, 180, doi: [10.3847/1538-3881/ac1582](https://doi.org/10.3847/1538-3881/ac1582)

Yoo, J., DePoy, D. L., Gal-Yam, A., et al. 2004, ApJ, 603, 139, doi: [10.1086/381241](https://doi.org/10.1086/381241)

Zang, W., Shvartzvald, Y., Udalski, A., et al. 2020, arXiv e-prints, arXiv:2010.08732. <https://arxiv.org/abs/2010.08732>

Zang, W., Hwang, K.-H., Udalski, A., et al. 2021a, AJ, 162, 163, doi: [10.3847/1538-3881/ac12d4](https://doi.org/10.3847/1538-3881/ac12d4)

Zang, W., Han, C., Kondo, I., et al. 2021b, Research in Astronomy and Astrophysics, 21, 239, doi: [10.1088/1674-4527/21/9/239](https://doi.org/10.1088/1674-4527/21/9/239)

Zhang, X., Zang, W., Udalski, A., et al. 2020, AJ, 159, 116, doi: [10.3847/1538-3881/ab6f6d](https://doi.org/10.3847/1538-3881/ab6f6d)